water

Article

Land Subsidence Assessment of an Archipelago Based on the InSAR Time Series Analysis Method

Deming Ma [1], Rui Zhao [2,*], Yongsheng Li [3] and Zhengguang Li [4]

[1] First Institute of Oceanography, Ministry of Natural Resources, Qingdao 266061, China
[2] State Nuclear Electric Power Planning Design & Research Institute Company Limited, Beijing 100095, China
[3] National Institute of Natural Hazards, Ministry of Emergency Management of China, Beijing 100085, China
[4] National Deep Sea Center, Ministry of Natural Resources, Qingdao 266237, China
* Correspondence: rui83@126.com

Abstract: The lack of resources on islands leads to their extremely rapid development, and this can result in frequent geological disasters involving island subsidence. These disasters not only destroy the ecological environment and landscape of islands but also pose massive threats to the safety of residents' lives and property and can even affect the country's maritime rights and interests. To meet the demands of island stability and safety monitoring, in this study, we propose a large-area, full-coverage deformation monitoring method using InSAR technology to assess island subsidence based on a comprehensive analysis of conventional monitoring techniques. The working principle and unique advantages of InSAR data are introduced, and the SBAS InSAR key interpretation processing flow are described in detail. The GPU-assisted InSAR processing method is used to improve the processing efficiency. The monitoring results showed that the southern island group of the Miaodao Archipelago was relatively stable overall, with an annual average deformation rate of 3 mm. Only a few areas experienced large-magnitude surface deformation, and the maximum annual deformation magnitude was 45 mm. The time series deformation results of the characteristic points of the five inhabited islands in the southern island group showed that the subsidence trends of the two selected points on Beichangshan Island (P1 and P2) were slowly declining. The P3 point on Nanchangshan Island experienced a large deformation, while the P4 point experienced a relatively small deformation. The selected points (P5, P6 and P7) on Miaodao Island, Xiaoheishan Island and Daheishan Island were stable during the monitoring period. InSAR data can be used to accurately identify the millimetre-scale microdeformations experienced by island groups, thus demonstrating the high-precision deformation monitoring capability of these data. In addition, the accuracy of these data can meet the needs of island and archipelago subsidence monitoring, and the proposed method is an effective means to monitor the spatial deformation of island targets. This study is conducive to further enriching and improving island stability and safety monitoring technology systems in China and to providing data and technical support for identifying and mastering potential island risks, protecting and utilizing islands and preventing and reducing disasters.

Keywords: InSAR; Miaodao Archipelago; surface subsidence monitoring; subsidence assessment; time series analysis

Citation: Ma, D.; Zhao, R.; Li, Y.; Li, Z. Land Subsidence Assessment of an Archipelago Based on the InSAR Time Series Analysis Method. *Water* **2023**, *15*, 465. https://doi.org/10.3390/w15030465

Academic Editors: Shui-Long Shen, J. Paul Liu, Chaoqi Zhu and Yonggang Jia

Received: 26 October 2022
Revised: 3 January 2023
Accepted: 18 January 2023
Published: 24 January 2023

1. Introduction

There are more than 11,000 islands in China's 3 million km^2 sea area, which is one of the countries with the largest number of islands in the world [1]. These islands are surrounded by the sea and have unique advantages in location, environment and resources. It is not only an important land and the second blue economic belt at sea, but also an important fulcrum for building marine ecological civilisations and building the Maritime Silk Road. It also plays an important role in safeguarding national maritime rights and interests and national defence security [2,3]. The islands along the coast of China are located west of the circum-Pacific seismic belt, one of the most rapid and sensitive interfaces affecting global change and land-sea interactions; this area is a typical vulnerable zone with frequent disasters [4,5]. Most of the islands are located far from the mainland and have fragile ecological environments. With the rapid development of the coastal economy and the lack of space resources, the development of islands has been crazily accelerated. This led to frequent geological disasters of the island land subsidence, which not only destroyed the original island ecological environment and landscape, but also caused losses to the lives and property safety of island residents [6]. At the same time, due to the relatively isolated island environment, disaster relief work is extremely difficult, which seriously restricts the development of the local economy and the improvement in the living standard of the islanders.

According to statistics, by the end of 2015, 425 districts and counties in 94 cities across the country of China had experienced land subsidence at a magnitude greater than 10 mm/a, and the total subsidence area had reached 120,000 square kilometres. Among these regions, 24 cities in 9 provinces had experienced serious subsidence of 50 mm/a, and the area affected by this serious subsidence was 5860 square kilometres. The losses caused by this subsidence are incalculable [7]. There have also been serious land subsidence disasters in other countries in the world, such as the United States, Italy, Germany, Poland, South Korea, India, etc. [8–13], as well as the delta areas of coastal cities [14,15], which have a huge impact on local production and life and even endanger people's lives and property security. The factors that cause land subsidence are also different, mainly including crustal movement, sea level rise, underground resource exploitation, excessive groundwater extraction and engineering environmental effects [16–32]. However, compared to developed countries, land subsidence in China occurs late, develops rapidly, lacks effective control measures and exhibits large annual rates [33]. The land subsidence development process is often irreversible, and once land subsidence conditions form, it is difficult for an area to recover [34]. Therefore, island land subsidence disasters have attracted increasing attention. In view of this increasingly serious situation, it is very urgent to monitor, evaluate and control island land subsidence effectively, and related work has important practical significance for follow-up disaster management. Reasonable and effective monitoring means can allow not only for the understanding and mastering of the evolution processes of island land subsidence deformation and damage, but it can also allow researchers to obtain the characteristics of land subsidence geological disasters, thus providing reliable data and a scientific basis for analysing and evaluating land subsidence, designing monitoring and early warning projects and ensuring effective governance to provide timely disaster prevention and mitigation measures to avoid and mitigate disasters. Based on this context, we took the southern island group of the Miaodao Archipelago, a typical high-intensity development region in Northern China, as the study area to conduct island subsidence monitoring and evaluation research.

Common methods used to monitor surface subsidence disasters mainly include traditional levelling, bedrock marker and layered marker measurements, global navigation satellite system (GNSS) monitoring, distributed optical fibre sensing technologies and airborne light detection and ranging (LiDAR). Levelling data have been recorded over a history lasting more than one hundred years. At present, this technology is still an important means of monitoring land subsidence. It is applicable for displacement monitoring research at different deformation stages. However, due to the influence of terrain and weather conditions, the work cycle is long, the continuous observation ability is poor and on-site measurements are required; thus, only a series of point shape variables can be obtained with this method. Bedrock benchmark measurements are currently recognised as the most reliable monitoring method. The accuracy, stability and sensitivity of the monitoring results obtained from bedrock markers and layered settlement markers are high, and the construction quality requirements of these data during the construction and monitoring process are also extremely strict [35,36]. GNSS technologies are used to monitor the position changes in some fixed points on the land surface, while the overall surface deformation can be reflected only through modelling. The limitation of this method is that serious multipath effects occur in mountainous areas where satellite signals are easily blocked, and monitoring points need to be arranged in advance when conducting on-site monitoring. Distributed optical fibre sensing technology is a new sensing technology that uses light as the carrier and optical fibre as the medium to sense and transmit external signals [37,38]. This method is suitable for performing the distributed and refined multiparameter monitoring of local land subsidence. Although the above monitoring methods can meet the accuracy requirements of deformation monitoring, they all have shortcomings, such as low observation point densities, and can provide only periodic, discontinuous on-site observations. Airborne LiDAR technology can be used to perform rapid, continuous, noncontact and full-coverage 3D deformation monitoring, but its application is affected by surface vegetation coverage and the monitoring environment of each analysed island, and the terrain surface conditions cannot be measured using LiDAR. Although these data can be postprocessed with various filtering methods, this shortcoming still affects the accuracy of the final results. Second, LiDAR scanning abilities are limited, and the deformation monitoring accuracy is affected in cases of bad weather, such as cloudy and rainy conditions. In addition, the application scope of LiDAR data has mainly focused on targeted small-scale geological hazard investigations and monitoring, and these data are not applicable for investigating geological hazards at large scales; additionally, it is also difficult to capture the early microdeformation of a disaster body using LiDAR data [39,40]. The deficiencies and defects of these existing technical means have seriously restricted the development of large-scale, high-precision island group surface subsidence monitoring [41]. With the development of synthetic aperture radar interferometry (InSAR) technology, continuous and large-scale ground observations have become a reality [42–48], thus offering a new method for monitoring island group ground subsidence.

InSAR is a space-to-Earth observation active remote sensing technology developed in the 1980s. With its outstanding advantages, including its all-weather monitoring capability, strong penetrability, high accuracy and high resolution when obtaining continuously covered surface elevation and information [49–54], InSAR has become a new advanced technology for surface deformation monitoring and has the ability to monitor surface deformation at a subcentimetre accuracy and at spatial resolutions ranging from decimetres to tens of metres. InSAR has been widely used by researchers in different fields of research over the decades since its development. InSAR has shown significant advantages in various fields of geoscience, including in research on volcanic eruptions [55–57], earthquakes [58–60], geological hazards [61–64], land subsidence [65–69], artificial bridge and building deformation [70,71] and surface deformation caused by underground resource exploitation [72,73]. InSAR can measure ground deformation at the regional scale [74] and even at the nationwide scale [75]. As these examples show, InSAR technology provides researchers with a reliable way of generating land deformation velocity fields. Compared to optical remote sensing techniques, InSAR can quantitatively monitor and characterise changes in surface natural environment morphology, reveal the slow change processes of the land surface and the potential risk events and compensate for the deficiencies of some conventional monitoring methods [76]. More importantly, InSAR, with its high-density measurement points and relatively short revisit period, can facilitate fine-scale expressions and characterisations of surface deformation monitoring objects over wide areas.

Although InSAR technology has been applied to many deformation monitoring fields, the method for monitoring the subsidence of small-scale islands has not been verified. At the same time, it is difficult to effectively identify the microdeformation due to the uncorrelation caused by the high vegetation coverage of the island. In addition, conventional InSAR processing methods and computing environments can hardly match advances in SAR satellite imaging techniques and data processing capabilities. Therefore, aiming at the needs of monitoring and evaluating the slow change in the subsidence of the islands, we proposed the application of the InSAR time series analysis method to monitor microdeformations for the land subsidence assessment of the archipelago. At the same time, a

GPU-assisted rapid InSAR time series analysis method targeting Sentinel-1 images was used to improve the processing efficiency based on the SBAS algorithm. In addition, the SBAS spatiotemporal filtering algorithm was employed to remove the atmospheric phase error in the case of the complex terrain and dense vegetation coverage of the archipelago. The proposed method was applied to map a small-scale surface deformation covering the southern island group of the Miaodao Archipelago. We carried out a fine-scale monitoring of unstable areas, focusing on the impact of aquaculture and other developments on surface deformation.

2. Materials and Methodology

2.1. Study Area

The southern island group of the Miaodao Islands is located at 37° 53.5′–38° 00.0′ N and 120° 35.2′–120° 45.6′ E, as shown in Figure 1. It is located in the north of the Jiaodong Peninsula at the intersection of the Yellow Sea and the Bohai Sea. It is an im-portant support for national key scenic spots and national nature reserves and enjoys the reputation of being a "Fairy Mountain on the Sea" and "Natural Oxygen Bar" [6]. The region belongs to the East Asian monsoon climate region, with an average annual temperature of 12.1 °C, an average annual precipitation total of 537.1 mm, an average annual relative humidity of 67% and an average annual sunshine duration of 2612 h. The main disastrous weather events affecting the islands in this region include cold waves, tropical cyclones, gales and droughts [77]. The southern island groups of the Miaodao Archipelago are bedrock islands, with the highest point at an elevation of approximately 195.7 m. The main geomorphic type is denuded hills. The soils mainly consist of brown soils containing many gravels, and they have a poor soil quality [78]. The southern island group of the Miaodao Archipelago is the political, economic and cultural centre of Changdao County. The degree of urban construction in this region is relatively high. With widespread mariculture areas and frequent transportation, tour-ism has become one of the important pillar industries of local economic development on these islands [79].

2.2. InSAR

2.2.1. InSAR Principle

InSAR technology involves the use of radars located in different spatial positions to observe the same target; these radars obtain two or more SAR images, and then interference processing is conducted to obtain the elevation or deformation information of the target [80,81]. Differential radar interferometry (D-InSAR) is usually used to monitor surface deformation. The interferometric phase calculation includes five parts as follows [82–84]:

$$\varphi_{InSAR} = \varphi_{orbit} + \varphi_{topography} + \varphi_{deformation} + \varphi_{atmosphere} + \varphi_{noise}$$

where φ_{orbit} represents the flat-ground phase or the reference plane phase, $\varphi_{topography}$ represents the terrain phase, $\varphi_{deformation}$ represents the deformation phase, $\varphi_{atmosphere}$ represents the atmospheric phase and φ_{noise} indicates the noise phase.

However, the D-InSAR method cannot be implemented in areas without a reference digital elevation model (DEM), and it is vulnerable to incoherence factors. In addition, D-InSAR monitoring results are also affected by satellite orbit errors, atmospheric errors and external DEM data errors, and there are certain limitations with regards to the application of long-term continuous deformation monitoring performed in the same area [85]. To solve the interference of various factors on the deformation monitoring results of D-InSAR technology, researchers have proposed time series InSAR technology to weaken the factor interference [49,86]. The main idea of temporal InSAR involves using multiscene SAR images taken in the same area to identify pixels with low spatiotemporal decoherence and then model and analyse the phases of these pixels to weaken the influence of phase errors and decoherence factors to obtain deformation monitoring results at a relatively high accuracy.

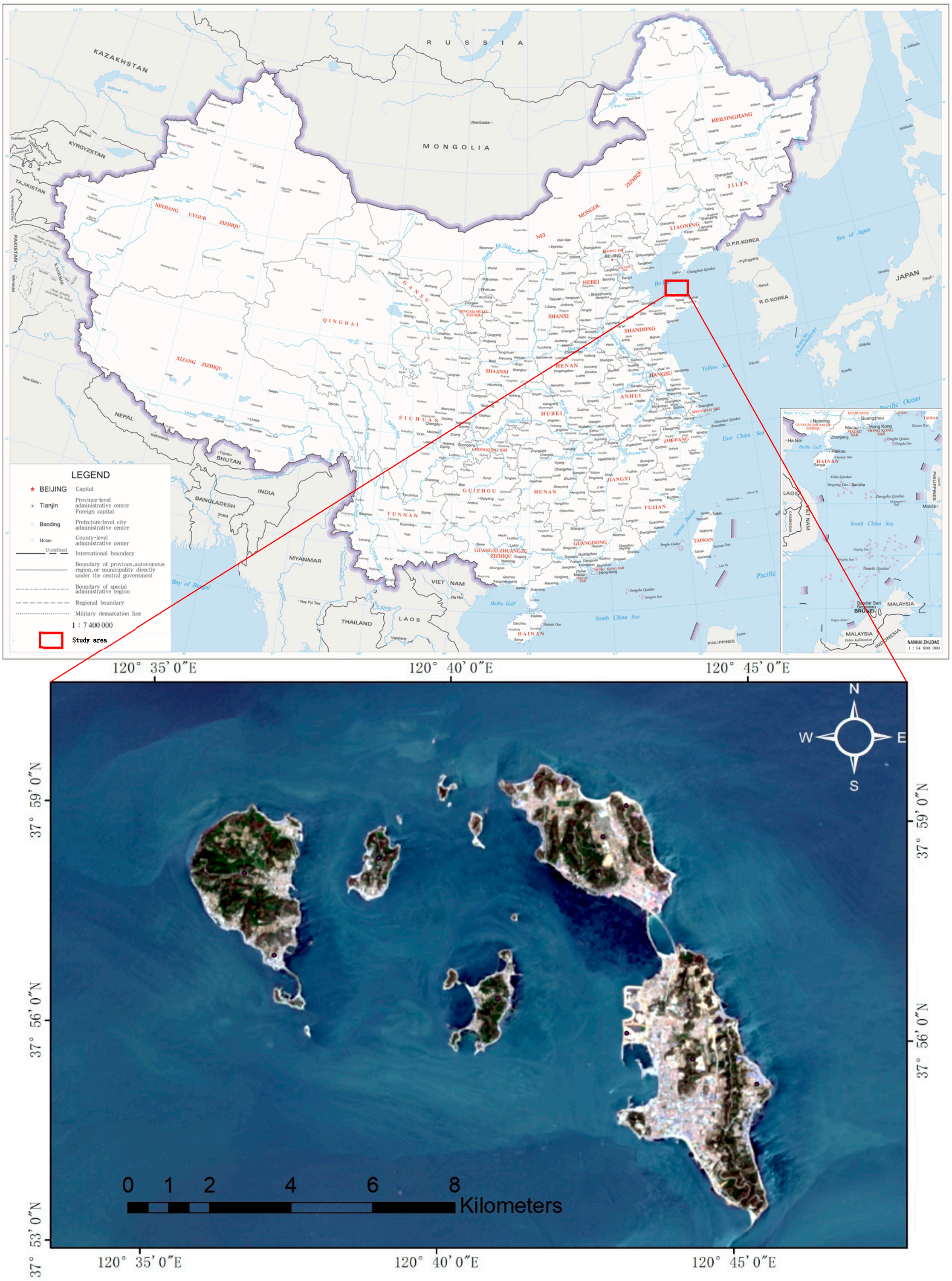

Figure 1. Location of the study area.

2.2.2. SBAS-InSAR

InSAR technology will lead to incoherent interferometry when the ground motion rate is significant, the environment changes significantly or the long baseline of interferometry pair. SBAS (Small Baseline Subset) InSAR combines all SAR images covering the same area into several subsets. The image baseline distance (including the temporal and spatial baseline) within the subset is small, and the baseline distance between subsets is significant [49]. Then, all available small baseline interferograms can be obtained by this strategy.

The deformation rate can be easily obtained using the singular value decomposition (SVD) method. The SBAS InSAR method suppresses the geometric decoherence caused by the long baseline and allows more SAR images to participate in deformation calculations, increasing the time sampling. In addition, the SBAS InSAR method generally performs multilook processing. In this way, the reduction in the spatial resolution also reduces the computational load and complexity of data processing at the expense of resolution [87]. The SBAS InSAR method has become reliable for monitoring slow surface displacement and has been widely used in different fields.

The original N + 1 SAR images can produce M unwrapped interferograms under the SBAS baseline constraint. The phase in point (x, y) of the i-th unwrapped interferogram (corresponding to the time t_1 and t_2) can be expressed as follows [88]:

$$\Delta\varphi_i(x,r) = \Delta\varphi_{t_2}(x,r) - \Delta\varphi_{t_1}(x,r) \approx \frac{4\pi}{\lambda}(d(t_2,x,r) - d(t_1,x,r))\Delta + \varphi^i_{top} + \Delta\varphi^i_{noise}$$

where $d(t_2, x, y)$ and $d(t_1, x, y)$ indicate the LOS deformation at the time t_1 and t_2. $\Delta\varphi^i_{top}$ is the residual phase derived from DEM inaccuracy. The $\Delta\varphi^i_{noise}$ represents the error phase from the atmospheric delay, unwrapped error and thermal noise. $\Delta\varphi_i$ is the phase of the i-th unwrapping interferogram and can be expressed as

$$\sum_{t_i,i+1}^{t_2,i} (t_p - t_{p-1})W = \Delta\varphi_i$$

where the parameter W to be solved are expressed as follows:

$$W^T = \left[W_1 = \frac{\varphi_1 - \varphi_0}{t_1 - t_0}, \cdots, W_N = \frac{\varphi_N - \varphi_{N-1}}{t_N - t_{N-1}}\right]$$

After removing the residual elevation phase and unwrapping error, the velocity phase is solved as follows:

$$AW = \Delta\varphi$$

where A is a matrix with dimensions of $M \times N$, and then the SVD algorithm with minimum norm conditions is introduced to obtain the deformation rate.

3. Research Area and Data Processing

3.1. Data Acquisition

(1) Satellite data

The C-band SAR image data of the Sentinel-1A satellite of the European Space Agency (ESA) were used to monitor the surface deformation of the southern island group of the Miaodao Archipelago. The monitoring period lasted from January 2018 to December 2020. See Table 1 for the specific parameters monitored. In addition, a Shuttle Radar Topography Mission (SRTM) DEM with a 30 m resolution was used as the reference DEM to estimate and remove the topographic phase.

A total of 248 ascending interferograms were generated using the short baseline set method, as shown in Figure 2. To reduce the volume of data to be processed and improve the processing efficiency, the data were divided according to the island location (red area refers to archipelago location), as shown in Figure 3. The red area in the figure is the position of the southern island group of the Miaodao Archipelago within the radar image.

Table 1. Sentinel-1A data parameters.

Id	Parameter	Value
1	Track Number	171
2	Frame	121
3	Imaging mode	Interference Wide Mode (IW Mode)
4	Angle of incidence/°	40
5	Polarisation mode	VV
6	Track alignment	Ascending
7	Range resolution/m	2.33
8	Azimuth resolution/m	13.90
9	Image data volume	87
10	Start time	29 January 2018
11	End time	8 December 2020

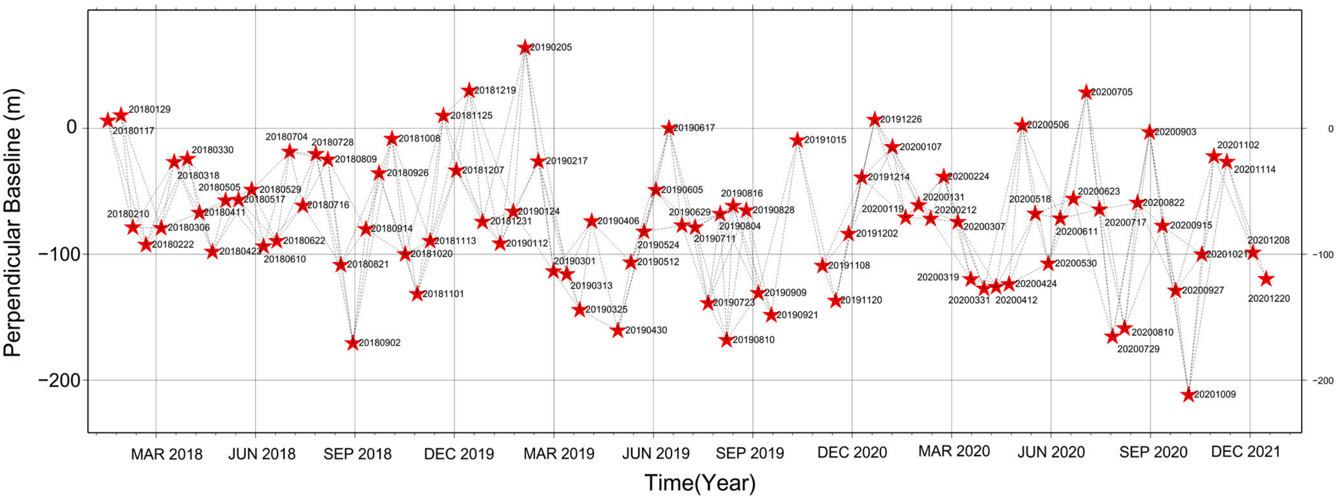

Figure 2. The small baseline network of ascending datasets (the pentagram represents each SAR image).

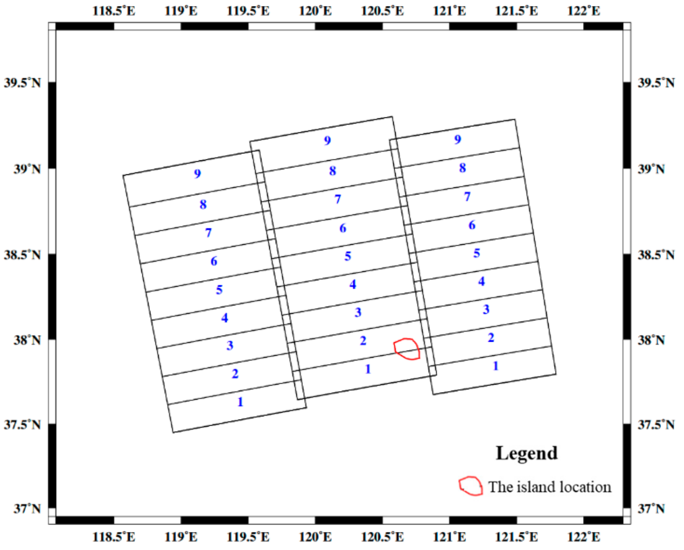

Figure 3. Data processing range (the number represents each burst sequence number).

3.2. Data Processing

The ground-settlement-monitoring data-processing flowchart of the southern island group of the Miaodao Archipelago based on SBAS InSAR technology is shown in Figure 4; this methodology can be divided into the following six steps:

(1) Primary reference image selection and baseline estimation

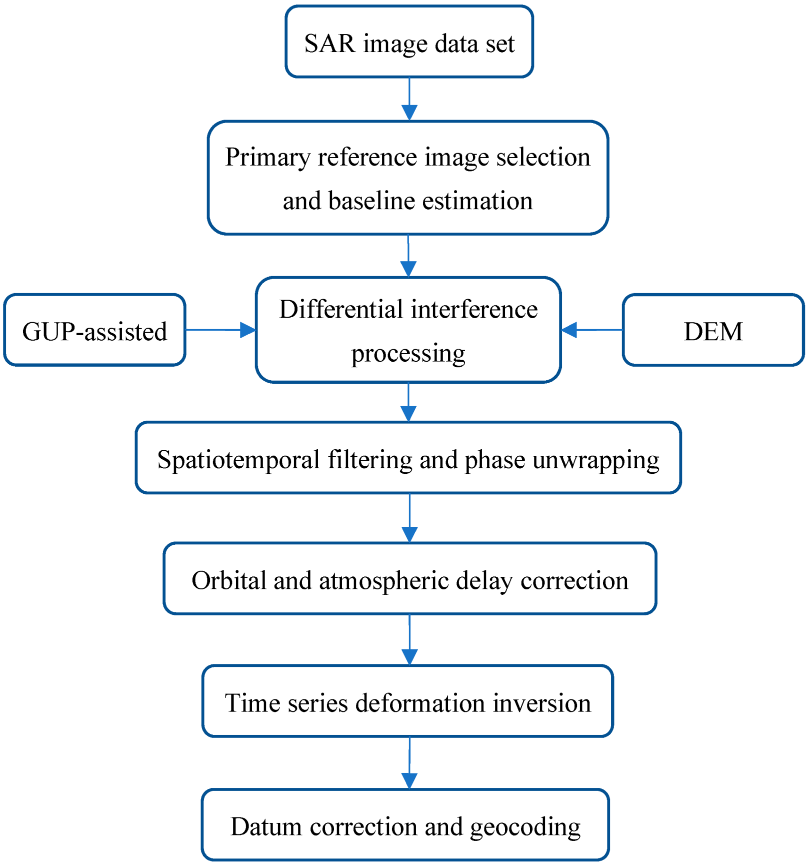

Figure 4. SBAS-InSAR data processing flow.

We calculated the baseline of all interferometric pairs so that the baseline generated by every pair of two SAR images was within the preset threshold; this method can indicate whether the images are coherent. Then, we generated the optimal spatiotemporal baseline connection diagram and interference pair connection diagram. Generally, the middle image of the time series was selected as the main reference image.

(2) Differential interference processing

First, we assessed and prepared precise orbit files and external DEM files for each image. The SRTM DEM with a 30 m resolution was used [89]. On the basis of existing interference processing methods, all differential interferograms were produced. This step is very time consuming, and we employed the graphics processing unit (GPU)-assisted InSAR processing method [90,91] to improve the processing efficiency; this process included geometric coregistration, resampling and ESD correction steps.

① In the geometric coregistration step, we used GPU-assisted technology to parallelise the repeated process of calculating the optimal correlation coefficient from multiple windows [90] and combined the precise geometric orbit positioning with the correlation coefficient registration method to improve the registration accuracy.

② After coregistration, we resampled a secondary image with the primary image. Before resampling, however, the linear Doppler centroid frequency of the secondary image had to be removed (deramping) to avoid aliasing. Additionally, the spectra of SAR data and interpolation convolution kernels had to be identically centred [92]. Accordingly, we performed deramping and demodulation at the same time [93] and used GPU assistance to improve the memory access efficiency [90].

③ To realise high-precision coregistration, enhanced spectral diversity (ESD) technology was used to fine tune the azimuth offsets derived from the geometric coregistration results [90,94]. ESD technology utilises the phase difference between the overlapping regions of adjacent bursts within a chosen subswath [91].

(3) Spatiotemporal filtering and phase unwrapping

A new SBAS spatiotemporal filtering algorithm was used to remove the atmospheric phase error in cases of complex terrain and dense vegetation coverage on the studied island group. The algorithm construction concept involved selecting the interference pairs that required the temporal and spatial baselines to be as short and small as possible to ensure the minimum effect of incoherence [91]. This spatiotemporal filtering method can effectively remove long wavelength signals in the spatial domain and short wavelength signals in the temporal time domain to provide a spatiotemporally continuous, high-precision deformation field. Then, the phase value in the interferogram was restored to the true value by phase unwrapping.

(4) Orbital and atmospheric delay correction

To reduce the orbital residual derived from possible inaccurate ephemeris parameters and tropospheric effects in the interferograms, we estimated a polynomial function to remove the estimated phase ramp [95]. The GACOS-assisted atmospheric delay error and long wavelength error correction had to be carried out before the stacking step was performed. By using redundant observations and stacking processing, the least squares method was applied to perform the deformation inversion of the unwrapped interferograms to estimate and weaken the atmospheric phase error and terrain error, allowing the deformation signal-to-noise ratio to be greatly improved.

(5) Time series deformation inversion

With high- and low-pass filters, the average deformation rate was calculated by employing the linear least squares (LS) method, and the time series cumulative deformation was then obtained via the SVD algorithm.

(6) Datum correction and geocoding

The time series deformation map and deformation rate map were transformed from the radar coordinate system to the geographic coordinate system.

4. Results and Discussion

4.1. Results

4.1.1. Land Subsidence Results and Distribution Characteristics of Island Groups

By using Sentinel-1A SAR data recorded from January 2018 to December 2020, the average deformation rate of the southern island group of the Miaodao Archipelago during this period was obtained through InSAR time series analysis. The results showed that the island group was relatively stable overall, as shown in Figure 5. Only a few coastal zones experienced slight deformation, and the average deformation rate was approximately 3 mm. Only in the western coastal zone of Nanchangshan Island was slightly significant surface subsidence observed, reaching 45 mm/yr.

4.1.2. Accuracy Evaluation of Monitoring Results

Due to the lack of GNSS and levelling monitoring data in the study area, it is impossible to evaluate the accuracy of the InSAR monitoring method proposed in this study through external data. So, to assess the reliability and consistency of the deformation rate measurements, we performed a cross-comparison of the observation results between the ascending and descending datasets. During the study period, a total of 142 descending interferograms were generated using the short baseline set method, as shown in Figure 6. Considering the geolocation-related mismatches between the pixels of these two datasets arising due to the dissimilar imaging geometries, we first selected 5773 points in the study area via grid sampling and then generated a scatterplot of the deformation rates derived from the two SAR datasets, as shown in Figure 7, revealing a high correlation of 0.95. The root mean square error (RMSE) of the differences reached 5.6 mm/year.

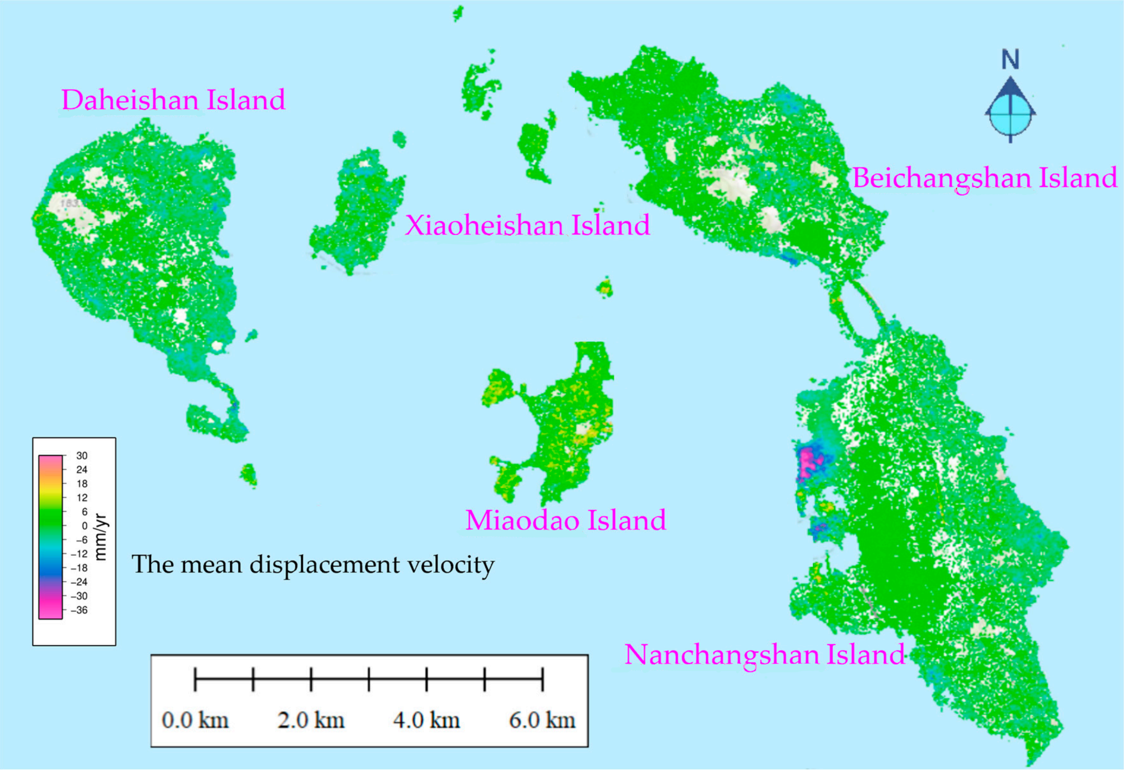

Figure 5. The mean displacement velocity map obtained based on Sentinel-1 data.

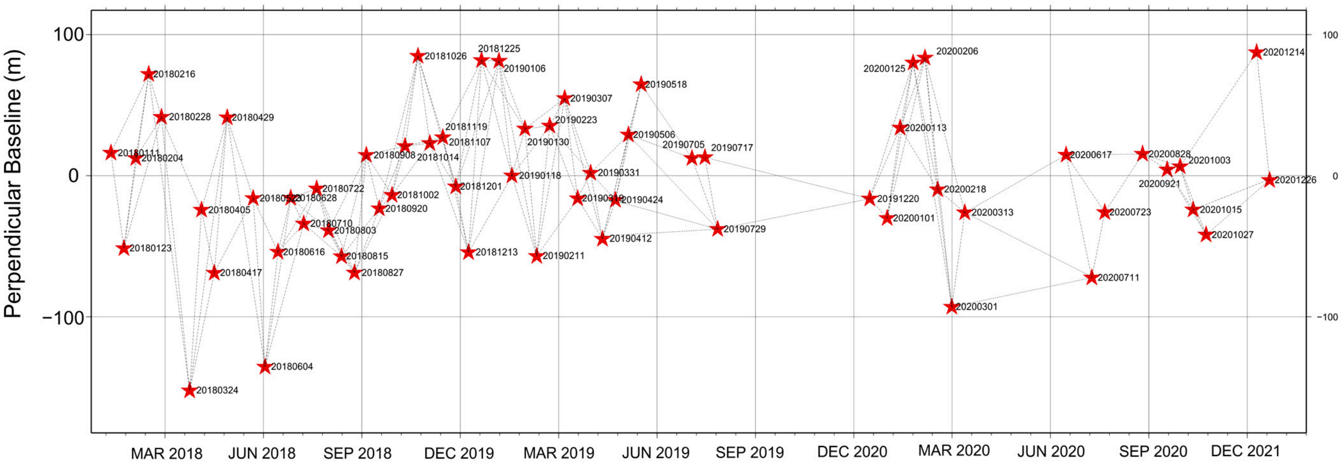

Figure 6. The small baseline network of descending datasets (the pentagram represents each SAR image).

4.1.3. Identification and Analysis of the Potential Settlement Points on the Analysed Archipelago

From Figure 8a, we can identify that obvious surface subsidence occurred on the west coast of Nanchangshan Island. After a detailed analysis of this area, we first enlarged the deformation field in this area to obtain the regional surface deformation distribution map, as shown in Figure 8b. The results showed that the surface deformation in this area was relatively large and occurred in an area in which construction was planned during the monitoring period, mainly due to the ground settlement caused by the ground construction. One of the points was selected for time series analysis (point P in Figure 8b), and the results showed that the point presented a continuous deformation feature from 2018 to the end of 2020 (Figure 9). The land subsidence in 2018 was approximately 40 mm, in 2019 was approximately 65 mm, in 2020 was approximately 30 mm and the total subsidence in three years was approximately 135 mm, with an average annual subsidence of approximately 45 mm.

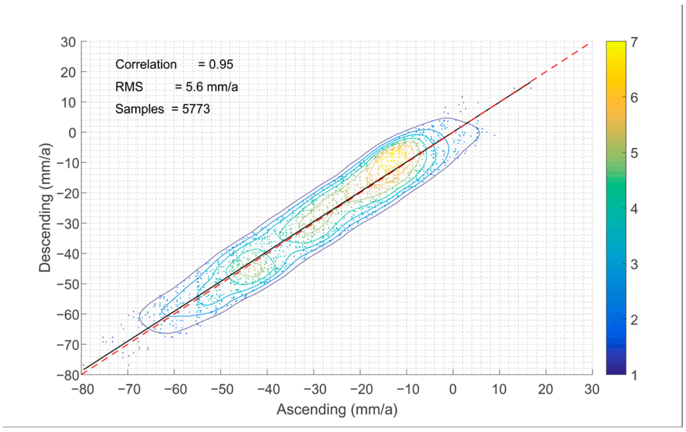

Figure 7. The cross-comparison results.

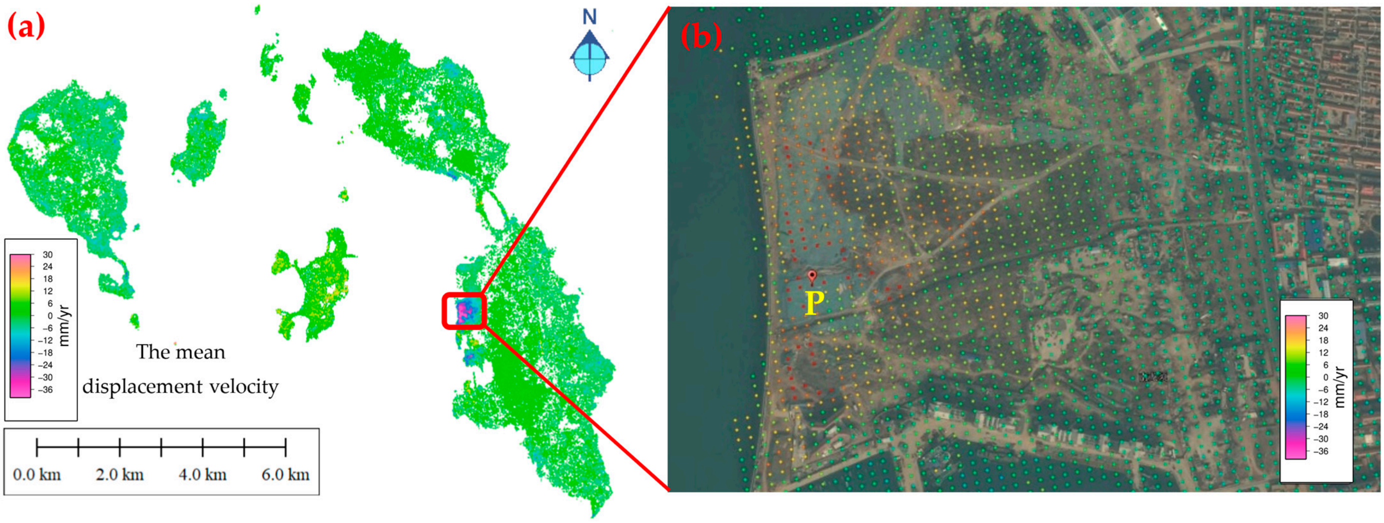

Figure 8. Identification of hidden danger points of Miaodao Archipelago. (**a**) The mean displacement velocity; (**b**) Enlarged view of areas with large mean displacement velocity.

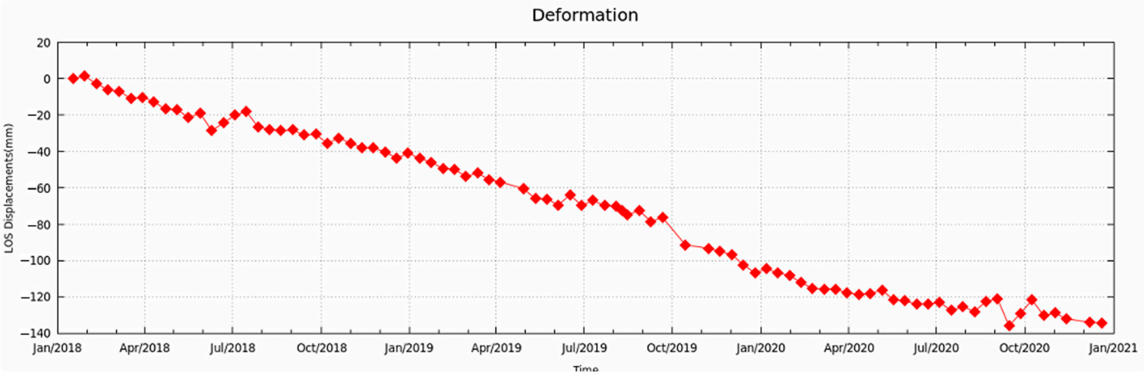

Figure 9. Time series deformation of target point.

4.1.4. Single-Point Time Series Results Analysis

To further analyse and evaluate the surface subsidence of the southern island group of the Miaodao Archipelago, we selected different characteristic points to perform a time series deformation analysis (as shown in Figure 10) on the five inhabited islands of the southern island group of the Miaodao Archipelago. The deformation monitoring results of each point are shown in Figures 11–17.

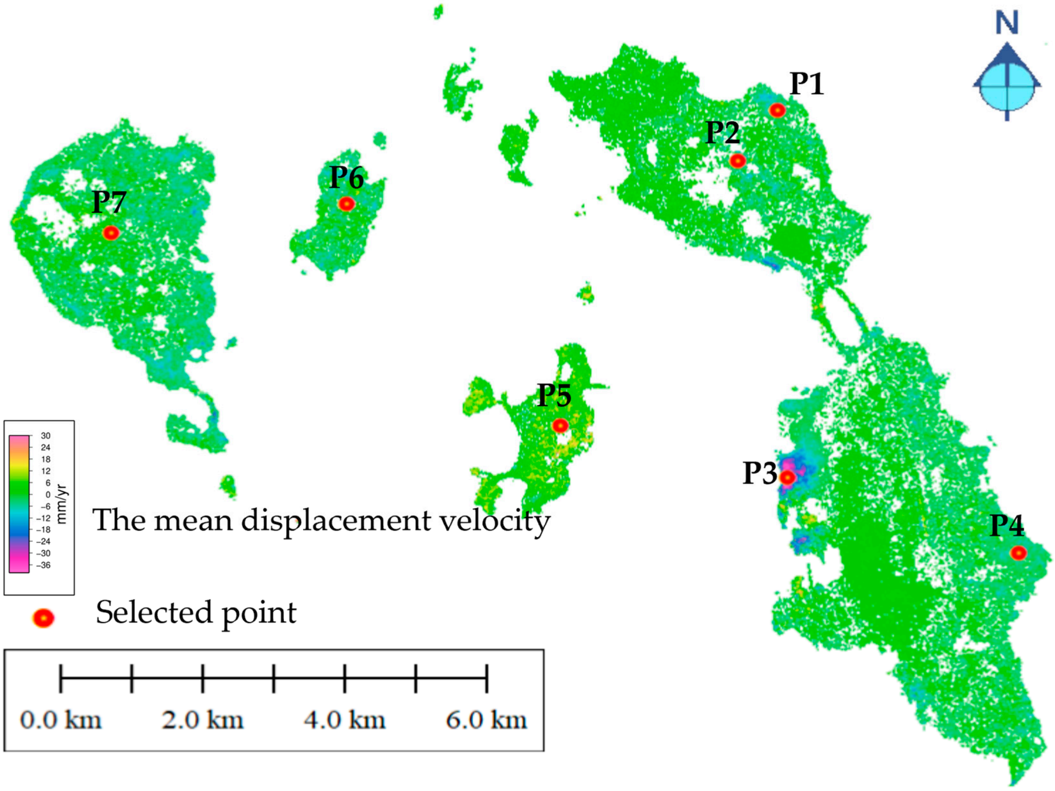

Figure 10. Sketch map of 9 selected points.

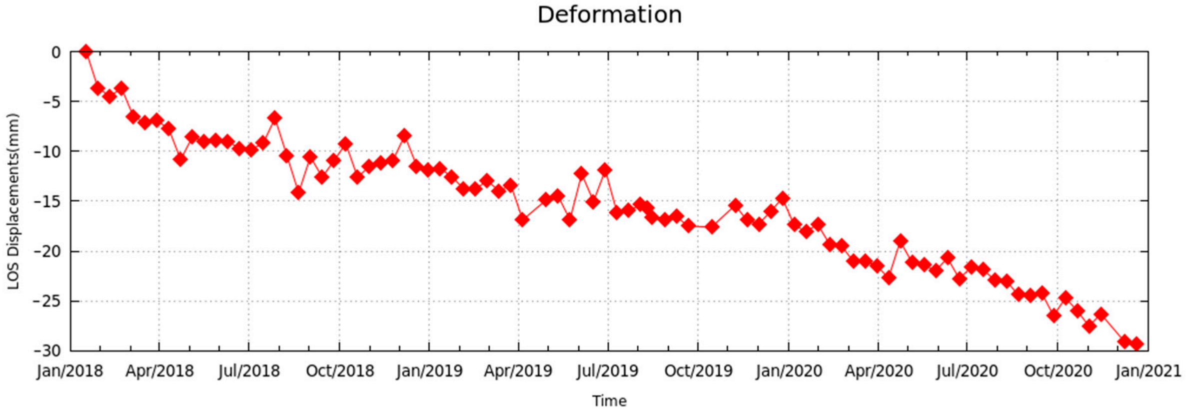

Figure 11. Deformation of point P1 during the monitoring period.

The two selected characteristic points (P1 and P2) of Beichangshan Island were in a state of microsettlement during the monitoring period. The three-year settlement magnitudes were 30 mm and 20 mm at points P1 and P2, respectively, and the annual settlement magnitudes were approximately 10 mm and 7 mm, respectively. Beichangshan Island, primarily, should thus monitor its subsidence changes in a timely manner. The two characteristic points (P3 and P4) selected for Nanchangshan Island were assessed; point P3 was located in an obvious settlement area and exhibited total settlement magnitudes of 120 mm and an annual settlement magnitude of 40 mm. The other point, P4, exhibited no obvious phase change and was relatively stable. Although the point selected for Miaodao Island (P5) exhibited a slight upwards trend, this trend may have been due to the error caused by forestland shielding, but the overall change was small. The P6 and P7 points selected for Xiaoheishan Island and Daheishan Island fluctuated around approximately 0 during the monitoring period and were thus stable.

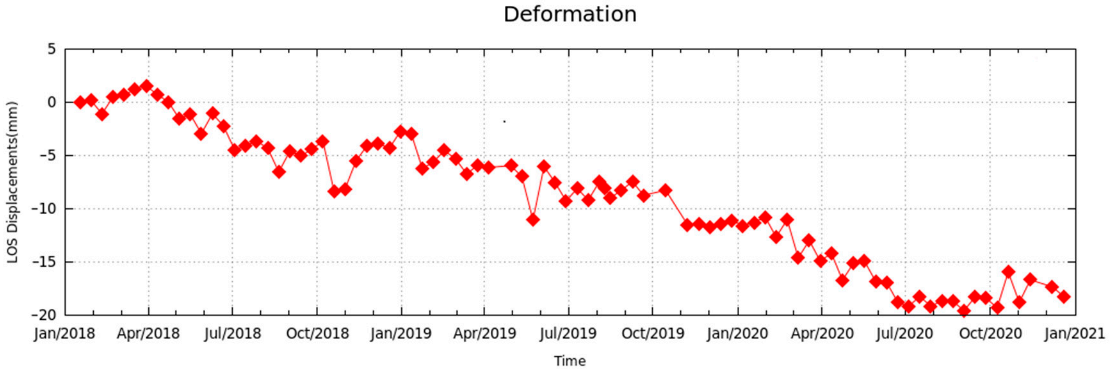

Figure 12. Deformation of point P2 during the monitoring period.

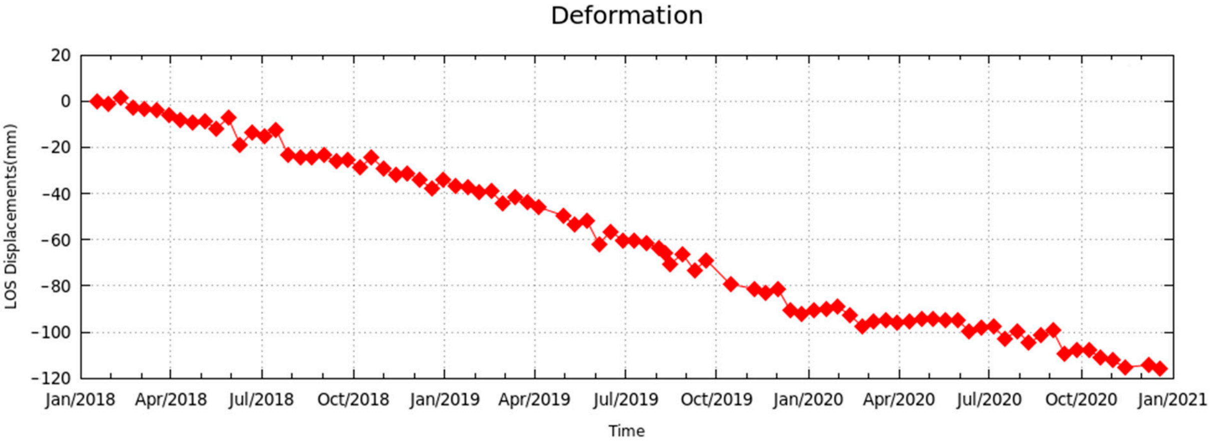

Figure 13. Deformation of point P3 during the monitoring period.

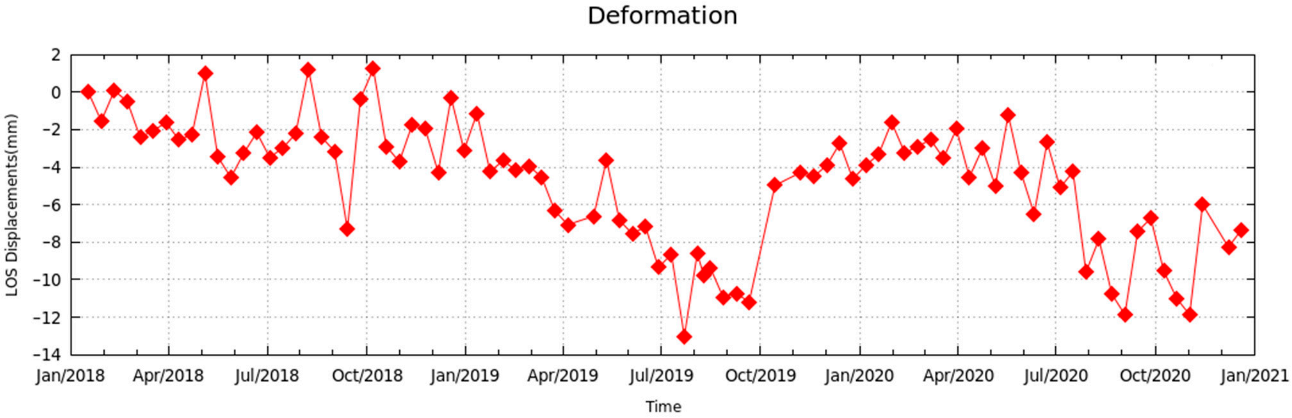

Figure 14. Deformation of point P4 during the monitoring period.

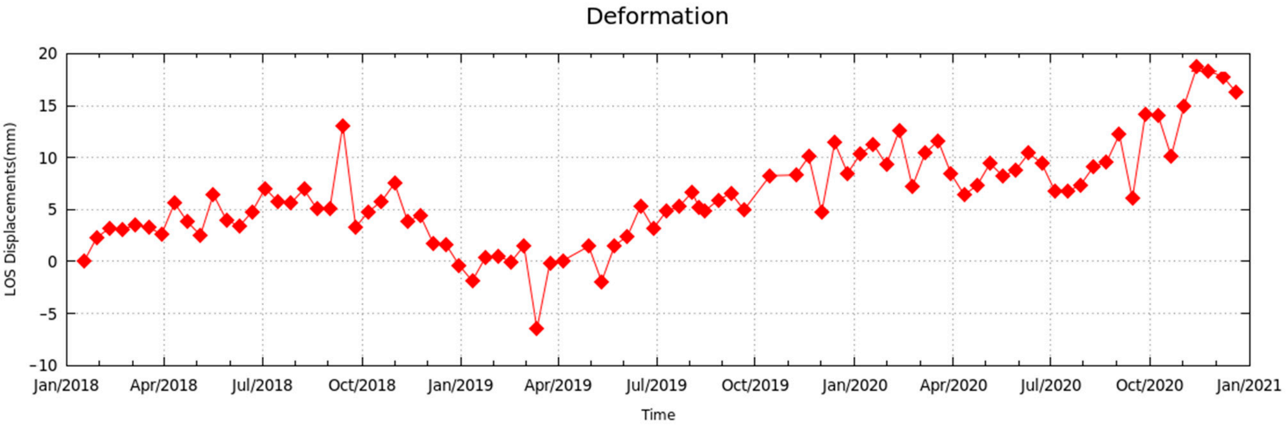

Figure 15. Deformation of point P5 during the monitoring period.

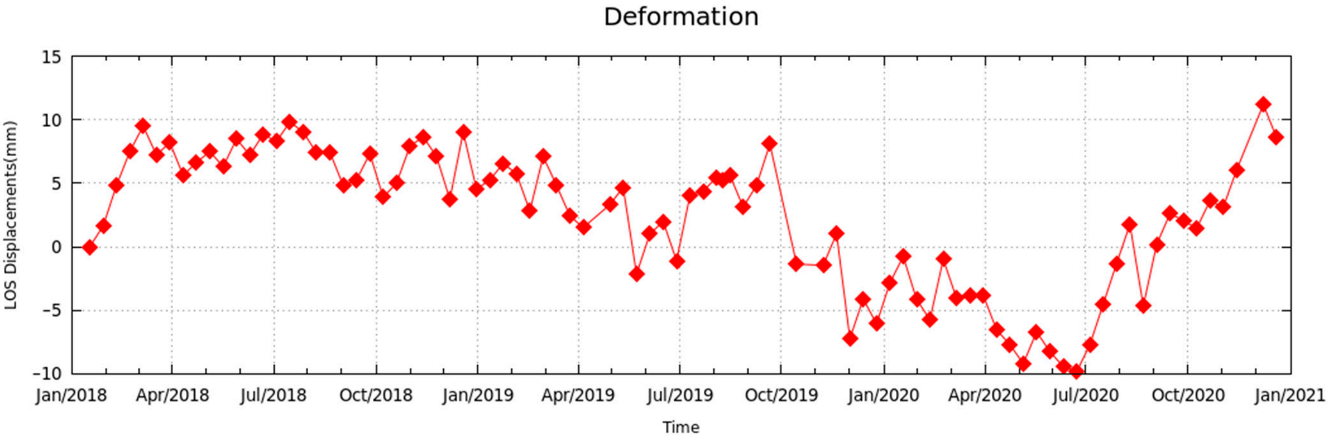

Figure 16. Deformation of point P6 during the monitoring period.

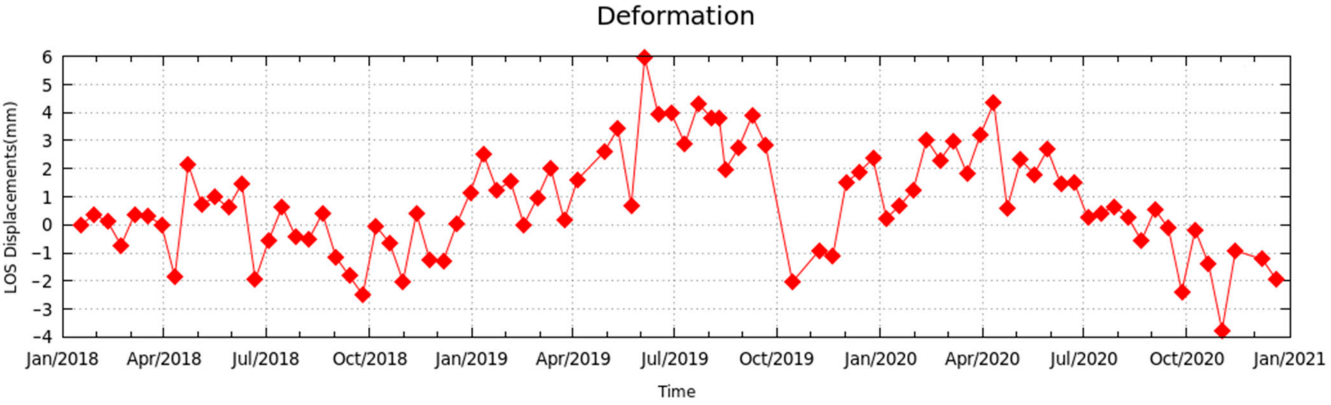

Figure 17. Deformation of point P7 during the monitoring period.

4.2. Discussion

4.2.1. Scalability Analysis of the Method

Studies have indicated that space-borne InSAR can monitor large-scale surface deformation [42–46]. We also proved that this technology can also be used to monitor the subsidence of islands on a small scale. At the same time, we solved the low coherence caused by the high vegetation coverage of the archipelago by using the time–space filtering method. This method promoted the accurate monitoring of complex scenes in the archipelago area, thus improving the accuracy of the results, and it could also be extended to the complex coastal areas.

Although we utilised both the ascending and descending orbit SAR images for cross-validation purposes, the mechanism of channel deformation was not comprehensive enough. Therefore, a joint solution involving InSAR and multisource SAR image/ground-based datasets such as GNSS or levelling is still crucial for the comprehensive analysis of the deformation mechanism and factors causing deformation.

4.2.2. Analysis of Factors Affecting Island Subsidence

There are many factors that cause land subsidence, including natural factors and human factors. Natural factors include earthquakes and sea level rise, and human factors include underground resource exploitation, excessive groundwater extraction and engineering construction. The investigation and study of island disasters in China shows that landslides, coastal erosion, the overexploitation of underground resources, reclamation projects, etc., are the main factors leading to island land subsidence [96]. From the deformation monitoring results of the southern islands of the Miaodao Archipelago, it can be seen that the main influencing factor for the occurrence of small areas with a relatively large deformation rate is the reclamation project in the aquaculture area. At the same time, this conjecture analysis was further verified in combination with a field survey, which also found the same deformation cause in the monitoring and research of other artificial islands [97].

In addition, there is a sandy coast in the southern island group of the Miaodao Archipelago, which is also a beautiful beach landscape. This type of coast is vulnerable to coastal erosion, so regular monitoring should be carried out, and ecological restoration should be carried out when necessary to avoid the island land subsidence caused by coastal erosion.

5. Conclusions

In this paper, to meet the needs of island group stability and safety monitoring, the InSAR time series analysis method was proposed to evaluate the microdeformation characteristics of island group land subsidence geological disasters, and the data processing method and framework are described in detail. At the same time, the GPU-assisted InSAR processing method was introduced to improve the processing efficiency and quickly obtain land subsidence deformation images of the southern island group of the Miaodao Archipelago during the monitoring period; the results verified the millimetre-level monitoring accuracy and the effectiveness of InSAR technologies. This study enriches the monitoring means of island land subsidence geological hazard research in China and is conducive to improving the island stability monitoring technology system and island safety monitoring capability in China. It provides a new technical means for the identification, early warning and prevention of the hidden danger of the island settlement disaster and avoids the loss of life and property caused by the island settlement to the maximum extent.

(1) InSAR technology can quickly realise the high-precision automatic monitoring of archipelago land subsidence through noncontact mode. It can not only obtain the deformation information of a single point, but also master the unstable state of the whole region and provide a continuous space–time deformation map of the monitoring region.
(2) InSAR can accurately identify the millimetre-scale microsettlement deformation characteristics of island groups and quickly obtain overall time series deformation images of the target, thus elucidating the high-precision deformation-monitoring capability of InSAR technology. The accuracy of this method meets the needs of island and archipelago settlement monitoring, and InSAR was shown to be an effective means for monitoring the spatial deformation characteristics of island targets.
(3) Through data processing and analyses, the deformation characteristics of the southern island group of the Miaodao Archipelago showed that the whole island group was in a stable state, and only a few areas showed large deformation due to ground construction; however, due to the slow surface settlement of Beishangshan Island,

this island should actively take effective measures to conduct regular monitoring and prevent potential sudden ground collapses that could cause losses.

(4) With the development of the big data era, realizing the effective fusion and integration of SAR images and other sensor data is the key to solving the problem of island group stability, and this will continue to be an important research topic in the future. Additionally, it is possible to gather some high-precision ground data, such as GNSS or levelling data, to confirm the accuracy of the monitoring results. We believe that the application prospects of InSAR technology will become increasingly diverse in the future.

Author Contributions: Conceptualization, D.M. and R.Z.; Data curation, D.M. and Y.L. Formal analysis, D.M., Y.L. and Z.L.; Investigation, D.M., Y.L. and Z.L.; Methodology, R.Z. and Y.L.; Project administration D.M. and R.Z.; Resources, R.Z. and Y.L.; Software, Y.L.; Supervision, D.M. and R.Z.; Visualization, Y.L.; Writing—original draft, D.M.; Writing—review & editing, D.M. All authors have read and agreed to the published version of the manuscript.

Funding: This research was funded by [the Public Science and Technology Research Funds Projects of Ocean, China] grant number [201405028] and [the marine industry standards of China] grant number [201810011-T].

Conflicts of Interest: The authors declare no conflict of interest.

References

1. Lu, H. *Special Report of the State Council of China on the Management of State-owned Natural Resources Assets in 2020*; State Council of China: Beijing, China, 2021.
2. Yang, B.J.; Lü, C.X. Protection, exploration and management of oceanic islands in China. *China Dev.* **2009**, *9*, 10–14.
3. Jiang, B.G.; Han, L.M. Scientifically exploiting island resources, and providing room for china's blue economic development. *J. Ocean. Univ. China (Soc. Sci. Ed.)* **2011**, *6*, 28–31.
4. Niu, W.Y. The discriminatory index with regard to the weakness, overlapness, and breadth of ecotone. *Acta Ecol. Sincica* **1989**, *9*, 97–105.
5. Xu, Y.Q.; Liu, L.J.; Li, P.Y.; Du, X.Y.; Li, P.; Zhang, X.L.; Gao, W. Geology disaster feature and genetic analysis of typical islands, China. *Acta Oceanol. Sin.* **2015**, *37*, 71–83.
6. Ma, D.; Li, Y.; Cai, J.; Li, B.; Liu, Y.; Chen, X. Real-Time diagnosis of island landslides based on GB-RAR. *J. Mar. Sci. Eng.* **2020**, *8*, 192. [CrossRef]
7. Zhang, L. Progress of InSAR Investigation and Monitoring of Land Subsidence in China. *Remote Sens. Land Resour.* **2017**, *1*, 91.
8. Ferretti, A.; Prati, C.; Rocca, F. Nonlinear subsidence rate estimation using permanent scatterers in differential SAR interferometry. *IEEE Transations Geosci. Remote Sens.* **2000**, *38*, 2202–2212. [CrossRef]
9. Farolfi, G.; Del Soldato, M.; Bianchini, S.; Casagli, N. A procedure to use GNSS data to calibrate satellite PSI data for the study of subsidence: An example from the north-western Adriatic coast (Italy). *Eur. J. Remote Sens.* **2019**, *52* (Suppl. S4), 54–63. [CrossRef]
10. Przyłucka, M.; Herrera, G.; Graniczny, M.; Colombo, D.; Béjar-Pizarro, M. Combination of Conventional and Advanced DInSAR to Monitor Very Fast Mining Subsidence with TerraSAR-X Data: Bytom City (Poland). *Remote Sens.* **2015**, *7*, 5300–5328. [CrossRef]
11. Przyłucka, M.; Kowalski, Z.; Perski, Z. Twenty years of coal mining-induced subsidence in the Upper Silesia in Poland identified using InSAR. *Int. J. Coal Sci. Technol.* **2022**, *9*, 86. [CrossRef]
12. Kapil, M.; Dheeraj, K.; Daniele, P.; Biswajeet, P. Estimation of ground subsidence of New Delhi, India using PS-InSAR technique and Multi-sensor Radar. *Adv. Space Res. Off. J. Comm. Space Res. (COSPAR)* **2022**, *4*, 69.
13. Yastika, P.E.; Shimizu, N.; Abidin, H.Z. Monitoring of long-term land subsidence from 2003 to 2017 in coastal area of Semarang, Indonesia by SBAS DInDAR analyses using Envisat-ASAR, ALOS-PALSAR, and Sentinel-1A SAR data. *Adv. Space Res.* **2019**, *63*, 1719–1736. [CrossRef]
14. Higgins, S.A.; Overeem, I.; Steckler, M.S.; Syvitski, J.P.M.; Seeber, L.; Akhter, S.H. InSAR measurements of compaction and subsidence in the Ganges-Brahmaputra Delta, Bangladesh. *J. Geophys. Res. Earth Surf.* **2015**, *119*, 1768–1781. [CrossRef]
15. Tessler, Z.D.; Vörösmarty, C.J.; Grossberg, M.; Gladkova, I.; Aizenman, H.; Syvitski, J.P.M.; Foufoula-Georgiou, E. Profiling risk and sustainability in coastal deltas of the world. *Science* **2015**, *349*, 638–643. [CrossRef] [PubMed]
16. Rateb, A.; Kuo, C.Y. Quantifying vertical deformation in the Tigris-Euphrates Basin due to the groundwater abstraction: Insights from GRACE and Sentinel-1 satellites. *Water* **2019**, *11*, 1658. [CrossRef]
17. Roosta, H.; Jalalifar, H.; Nasab, S.K.; Ranjbar, M. Surface deformation over the buried Nasr Abad salt diapir, Central Iran using interferometric synthetic aperture radar data. *Int. J. Remote Sens.* **2019**, *40*, 1–20. [CrossRef]
18. Mohan, R.; Herrington, T. Coastal resiliency considerations for America's four coasts: Preparing for 2100. *J. Mar. Environ. Eng.* **2021**, *10*, 319–330.

19. Solarski, M. Anthropogenic transformations of the Bytom area relief in the period of 1883–1994. *Environ. Socio-Econ. Stud.* **2013**, *1*, 1–8. [CrossRef]
20. Akcin, H.; Kutoglu, H.S.; Kemaldere, H.; Deguchi, T.; Koksal, E. Monitoring subsidence effects in the urban area of Zonguldak Hardcoal Basin of Turkey by InSAR-GIS integration. *Nat. Hazards Earth Syst. Sci.* **2010**, *10*, 1807–1814. [CrossRef]
21. Marschalko, M.; Yilmaz, I.; Křístková, V.; Fuka, M.; Kubečka, K.; Bouchal, T. An indicative method for determination of the most hazardous changes in slopes of the subsidence basins in underground coal mining area in Ostrava (Czech Republic). *Environ. Monit. Assess.* **2013**, *185*, 509–522. [CrossRef]
22. Kaneko, S.; Toyota, T. Long-term urbanization and land subsidence in Asian megacities: An indicators system approach. In *Groundwater and Subsurface Environments: Human Impacts in Asian Coastal Cities*; Taniguchi, M., Ed.; Springer: Tokyo, Japan, 2011; pp. 249–270.
23. Nyssen, J.; Vermeersch, D. Slope aspect affects geomorphic dynamics of coal mining spoil heaps in Belgium. *Geomorphology* **2010**, *123*, 109–121. [CrossRef]
24. Hrishikesh, K.; Tajdarul, H.S.; Falk, A.; Ritesh, A.; Venkatesh, A.S. Space-time evolution of land subsidence in the National capital Region of India using ALOS-1 and Sentinel-1 SAR data: Evidence for groundwater overexploitation. *J. Hydrol.* **2022**, *605*, 127329.
25. Nicholls, R.J.; Lincke, D.; Hinkel, J.; Brown, S.; Vafeidis, A.T.; Meyssignac, B.; Hanson, S.E.; Merkens, J.L.; Fang, J. A global analysis of subsidence, relative sea-level change and coastal flood exposure. *Nat. Claimate Chang.* **2021**, *11*, 338–342. [CrossRef]
26. Ciampalini, A.; Solari, L.; Giannecchini, R.; Galanti, Y.; Moretti, S. Evaluation of subsidence induced by long-lasting buildings load using InSAR technique and geotechnical data: The case study of a Freight Terminal (Tuscany, Italy). *Int. J. Appl. Earth Obs. Geoinf.* **2019**, *82*, 101925. [CrossRef]
27. Métois, M.; Benjelloun, M.; Lasserre, C.; Grandin, R.; Barrier, L.; Dushi, E.; Koci, R. Subsidence associated with oil extraction, measured from time series analysis of Sentinel-1 data: Case study of the Patos-Marinza oil field, Albania. *Solid Earth* **2020**, *11*, 363–378. [CrossRef]
28. Lee, D.K.; Mojtabai, N.; Lee, H.B.; Song, W.K. Assessment of the influencing factors on subsidence at abandoned coal mines in South Korea. *Environ. Earth Sci.* **2013**, *68*, 647–654. [CrossRef]
29. Dang, V.K.; Nguyen, T.D.; Dao, N.H.; Duong, T.L.; Dinh, X.V.; Weber, C. Land subsidence induced by underground coal mining at Quang Ninh, Vietnam: Persistent scatterer interferometric synthetic aperture radar observation using Sentinel-1 data. *Int. J. Remote Sens.* **2021**, *42*, 3563–3582. [CrossRef]
30. Harnischmacher, S.; Zepp, H. Mining and its impact on the earth surface in the Ruhr District (Germany). *Z. Fur Geomorphol.* **2014**, *58* (Suppl. S3), 3–22. [CrossRef]
31. Chaussard, E.; Amelung, F.; Abidin, H.; Hong, S.H. Sinking Cities in Indonesia: ALOS-PALSAR detects rapid subsidence due to groundwater and gas extraction. *Remote Sens. Environ.* **2013**, *128*, 150–161. [CrossRef]
32. Solarski, M.; Machowski, R.; Rzetala, M.; Rzetala, M.A. Hypsometric changes in urban areas resulting from multiple years of mining activity. *Sci. Rep.* **2022**, *12*, 2982. [CrossRef]
33. Yin, Y.P.; Zhang, Z.C.; Zhang, K.J. Land subsidence and countermeasures for its prevention in China. *The Chinese J. Geol. Hazard Control.* **2005**, *16*, 1–8.
34. Qin, T.C.; Cheng, G.M.; Wang, H.G. The latest progress of research on land subsidence abroad and its inspiration to China. *Geol. Bull. China* **2018**, *37*, 503–509.
35. Phien-Wej, N.; Giao, P.H.; Nutalaya, P. Land subsidence in Bangkok, Thailand. *Eng. Geol.* **2006**, *82*, 187–201. [CrossRef]
36. Qi, B.; Niu, W.M. A technological study of the monitoring system for layer wise mark in the Tianjin Binhai New Area. *Hydrogeol. Eng. Geol.* **2011**, *38*, 44–48.
37. Schenato, L.; Galtarossa, A.; Pasuto, A.; Palmieri, L. Distributed optical fiber pressure sensors. *Opt. Fiber Technol.* **2020**, *58*, 102239. [CrossRef]
38. Mekhtiev, A.D.; Sarsikeev, E.Z.; Neshina, E.G.; Kina, A.A.D.; Musagazhinov, M.Z. A Quasi-Distributed Fiber-Optical Monitoring System for Movement of Roof Strata in Mines. *J. Min. Sci.* **2022**, *58*, 338–346. [CrossRef]
39. Khan, S.D.; Huang, Z.; Karacay, A. Study of ground subsidence in northwest Harris county using GPS, LiDAR, and InSAR techniques. *Nat. Hazards* **2014**, *73*, 1143–1173. [CrossRef]
40. Zhang, Q.; Huang, G.; Yang, C. Precision space observation technique for geological hazard monitoring and early warning. *Acta Geod. Et Cartogr. Sin.* **2017**, *46*, 1300–1307.
41. Zhu, J.J.; Li, Z.W.; Hu, J. Research progress and methods of InSAR for deformation monitoring. *Acta Geod. Et Cartogr. Sin.* **2017**, *46*, 1717–1733.
42. Bürgmann, R.; Rosen, P.A.; Fielding, E.J. Synthetic aperture radar interferometry to measure earth's surface topography and its deformation. *Annu. Rev. Earth Planet. Sci.* **2000**, *28*, 169–209. [CrossRef]
43. Del Soldato, M.; Confuorto, P.; Bianchini, S.; Sbarra, P.; Casagli, N. Review of Works Combining GNSS and InSAR in Europe. *Remote Sens.* **2021**, *13*, 1684. [CrossRef]
44. Parizzi, A.; Brcic, R.; Zan, F.D. InSAR Performance for Large-Scale Deformation Measurement. *IEEE Trans. Geosci. Remote Sens.* **2021**, *59*, 8510–8520. [CrossRef]
45. Michael, H.; Mohamed, A.; Esayas, G.; Dorina, M.; Michael, S. Land subsidence in the Texas coastal bend: Locations, rates, triggers, and consequences. *Remote Sens.* **2022**, *14*, 192.

46. Hussain, M.A.; Chen, Z.; Shoaib, M.; Shah, S.U.; Khan, J.; Ying, Z. Land subsidence of coastal city of Pakistan using persistent scatterers In-SAR technique. *Sci. Rep.* **2022**, *12*, 5294. [CrossRef]
47. Liao, M.S.; Lin, H. *Synthetic Aperture Radar Interferometry: Principle and Signal Processing*; Surveying and Mapping Publishing House: Beijing, China, 2003; pp. 1–2.
48. Zhang, Y.H.; Liu, B.; Wu, H.A.; Cheng, X.; and Kang, Y.H. Ground subsidence in Xiong'an new area from 2012 to 2016 monitored by InSAR technique. *J. Earth Sci. Environ.* **2018**, *40*, 652–662.
49. Berardino, P.; Fornaro, G.; Lanari, R.; Sansosti, E. A new algorithm for surface deformation monitoring based on small baseline differential SAR interferograms. *IEEE Trans. Geosci. Remote Sens.* **2002**, *40*, 2375–2383. [CrossRef]
50. Perissin, D.; Wang, T. Time-Series InSAR Applications Over Urban Areas in China. *IEEE J. Sel. Top. Appl. Earth Obs. Remote Sens.* **2011**, *4*, 92–100. [CrossRef]
51. Herrera, G.; Gutiérrez, F.; García-Davalillo, J.C.; Guerrero, J.; Notti, D.; Galve, J.P.; Fernández-Merodo, J.A.; Cooksley, G. Multi-sensor advanced DInSAR monitoring of very slow landslides: The Tena Valley case study(Central Spanish Pyrenees). *Remote Sens. Environ.* **2013**, *128*, 31–43. [CrossRef]
52. Nagler, T.; Rott, H.; Kamelger, A. Analysis of Landslides in Alpine Areas by Means of SAR Interferometry. In Proceedings of the IEEE International Geoscience and Remote Sensing Symposium, Toronto, ON, Canada, 24–28 June 2002.
53. Wang, T.; Perissin, D.; Liao, M.; Rocca, F. Deformation Monitoring by Long Term D-InSAR Analysis in Three Gorges Area, China. In Proceedings of the IEEE International Geoscience and Remote Sensing Symposium, Boston, MA, USA, 8–11 July 2008.
54. Ferretti, A.; Savio, G.; Barzaghi, R.; Borghi, A.; Musazzi, S.; Novali, F.; Prati, C.; Rocca, F. Submillimeter accuracy of InSAR time series: Experimental validation. *IEEE Trans. Geosci. Remote Sens.* **2007**, *45*, 1142–1153. [CrossRef]
55. Hooper, A.; Zebker, H.; Segall, P.; Kampes, B. A new method for measuring deformation on volcanoes and other natural terrains using InSAR persistent scatterers. *Geophys. Res. Lett.* **2004**, *31*, L23611. [CrossRef]
56. Hooper, A.; Prata, F.; Sigmundsson, F. Remote sensing of volcanic hazards and their precursors. *Proc. IEEE* **2012**, *100*, 2908–2930. [CrossRef]
57. Lee, C.W.; Lu, Z.; Jung, H.S.; Won, J.S.; Dzurisin, D. Surface deformation of Augustine Volcano, 1992–2005, from multiple interferogram processing using a refined small baseline subset(SBAS). The 2006 eruption of Augustine Volcano, Alaska. *USGS Prof. Pap.* **2010**, *1769*, 453–465.
58. Shanker, P.; Casu, F.; Zebker, H.A.; Lanari, R. Comparison of persistent scatterers and small baseline Time-Series InSAR results: A case study of the San Francisco Bay area. *IEEE Geosci. Remote Sens. Lett.* **2011**, *8*, 592–596. [CrossRef]
59. Béjar-Pizarro, M.; Álvarez Gómez, J.A.; Staller, A.; Luna, M.P.; Pérez-López, R.; Monserrat, O.; Chunga, K.; Lima, A.; Galve, J.P.; Martínez Díaz, J.J.; et al. InSAR-Based Mapping to Support Decision-Making after an Earthquake. *Remote Sens.* **2018**, *10*, 899. [CrossRef]
60. Massonnet, D.; Rossi, M.; Carmona, C.; Adragna, F.; Peltzer, G.; Feigl, K.; Rabaute, T. The displacement field of the Landers earthquake mapped by radar interferometry. *Nature* **1993**, *364*, 138–142. [CrossRef]
61. Novellino, A.; Cigna, F.; Sowter, A.; Ramondini, M.; Calcaterra, D. Exploitation of the intermittent SBAS (ISBAS) algorithm with COSMO-SKYMED data for landslide inventory mapping in north-western Sicily, Italy. *Geomorphology* **2017**, *280*, 153–166. [CrossRef]
62. Ambrosi, C.; Strozzi, T.; Scapozza, C.; Wegmüller, U. Landslide hazard assessment in the Himalayas (Nepal and Bhutan) based on Earth-Observation data. *Eng. Geo.* **2018**, *237*, 217–228. [CrossRef]
63. Wasowski, J.; Bovenga, F. Investigating landslides and unstable slopes with satellite multi temporal interferometry: Current issues and future perspectives. *Eng. Geol.* **2014**, *174*, 103–138. [CrossRef]
64. Carlà, T.; Intrieri, E.; Raspini, F.; Bardi, F.; Farina, P.; Ferretti, A.; Colombo, D.; Novali, F.; and Casagli, N. Perspectives on the prediction of catastrophic slope failures from satellite InSAR. *Sci. Rep.* **2019**, *9*, 14137. [CrossRef]
65. Cigna, F.; Osmanŏglu, B.; Cabral-Cano, E.; Dixon, T.H.; Ávila-Olivera, J.A.; Garduno- Monroy, V.H.; DeMets, C.; Wdowinski, S. Monitoring land subsidence and its induced geological hazard with synthetic aperture radar interferometry: A case study in Morelia, Mexico. *Remote Sens. Environ.* **2012**, *117*, 146–161. [CrossRef]
66. Abidin, H.Z.; Andreas, H.; Gumilar, I.; Yuwono, B.D.; Murdohardono, D.; Supriyadi, S. On integration of geodetic observation results for assessment of land subsidence hazard risk in urban areas of Indonesia. In *IAG 150 Years*; Springer: Cham, Switzerland, 2016; Volume 143, pp. 435–442.
67. Armas, I.; Mendes, D.A.; Popa, R.G.; Gheorghe, M.; Popovici, D. Long-term ground deformation patterns of Bucharest using multitemporal InSAR and multivariate dynamic analyses: A possible transpressional system? *Sci. Rep.* **2017**, *7*, 43762. [CrossRef] [PubMed]
68. Motagh, M.; Shamshiri, R.; Haghshenas Haghighi, M.; Wetzel, H.U.; Akbari, B.; Nahavandchi, H.; Roessner, S.; Arabi, S. Quantifying groundwater exploitation induced subsidence in the Rafsanjan plain, southeastern Iran, using InSAR time-series and in situ measurements. *Eng. Geol.* **2017**, *218*, 134–151. [CrossRef]
69. Strozzi, T.; Caduff, R.; Wegmüller, U.; Raetzo, H.; Hauser, M. Widespread surface subsidence measured with satellite SAR interferometry in the Swiss Alpine range associated with the construction of the Gotthard Base Tunnel. *Remote Sens. Environ.* **2017**, *190*, 1–12. [CrossRef]
70. Erten, E.; Rossi, C. The worsening impacts of land reclamation assessed with Sentinel-1: The Rize (Turkey) test case. *Int. J. Appl. Earth Obs. Geoinf.* **2019**, *74*, 57–64. [CrossRef]

71. Selvakumaran, S.; Rossi, C.; Marinoni, A.; Webb, G.; Bennetts, J.; Barton, E.; Plank, S.; Middleton, C. Combined InSAR and terrestrial structural monitoring of bridges. *IEEE Trans. Geosci. Remote Sens.* **2020**, *58*, 7141–7153. [CrossRef]
72. Zerbini, S.; Richter, B.; Rocca, F.; Van Dam, T.; Matonti, F. A Combination of Space and Terrestrial Geodetic Techniques to Monitor Land Subsidence: Case Study, the Southeastern Po Plain, Italy. *J. Geophys. Res.* **2007**, *112*, B05401. [CrossRef]
73. Nádudvari, A. Using radar interferometry and SBAS technique to detect surface subsidence relating to coal mining in Upper Silesia from 1993–2000 and 2003–2010. *Environ. Socio-Econ. Stud.* **2016**, *4*, 24–34. [CrossRef]
74. Raspini, F.; Bianchini, S.; Ciampalini, A.; Del Soldato, M.; Solari, L.; Novali, F.; Del Conte, S.; Rucci, A.; Ferretti, A.; Casagli, N. Continuous, semi-automatic monitoring of ground deformation using Sentinel-1 satellites. *Sci. Rep.* **2018**, *8*, 7253. [CrossRef]
75. Costantini, M.; Ferretti, A.; Minati, F.; Falco, S.; Trillo, F.; Colombo, D.; Novali, F.; Malvarosa, F.; Mammone, C.; Vecchioli, F.; et al. Analysis of surface deformations over the whole Italian territory by interferometric processing of ERS, Envisat and COSMO-SkyMed radar data. *Remote Sens. Environ.* **2017**, *202*, 250–275. [CrossRef]
76. Strozzi, T.; Klimeš, J.; Frey, H.; Caduff, R.; Huggel, C.; Wegmüller, U.; and Rapre, A.C. Satellite SAR interferometry for the improved assessment of the state of activity of landslides: A case study from the Cordilleras of Peru. *Remote Sens. Environ.* **2018**, *217*, 111–125. [CrossRef]
77. Compilation Committee of China Island Records. *China Island Records Shandong Volume 1 (North Coast of Shandong Province)*; China Ocean Press: Beijing, China, 2013.
78. Shi, H.H.; Wang, X.L.; Wang, A.; Liu, Z.Y.; Ma, D.M. Storage and drivers of forests carbon on the Beichangshan Island of Miaodao Archipelago. *Acta Ecol. Sin.* **2013**, *33*, 6363–6372.
79. Chi, Y.; Shi, H.; Wang, Y.; Guo, Z.; Ma, D. Evaluation on spatial heterogeneity of island ecosystem carrying capacity-A case study of southern Midaodao Archipelago. *China Environ. Sci.* **2017**, *37*, 1188–1200.
80. Zebker, H.A.; Werner, C.L.; Rosen, P.A.; Hensley, S. Accuracy of topographic maps derived from ERS-1 interferometric radar. *IEEE Trans. Geosci. Remote Sens.* **1994**, *32*, 823–836. [CrossRef]
81. Hanssen, R.F. *Radar Interferometry Data Interpretation and Error Analysis*; Springer: Delft, The Netherlands, 2001.
82. Costantini, C.; Ferretti, A.; Prati, C.; Rocca, F. Monitoring landslides and tectonic motions with the permanent scatterers technique. *Eng. Geol.* **2003**, *68*, 31–34.
83. Liu, G.X. *Monitoring of Ground Deformations with Radar Interferometry*; Surveying and Mapping Press: Beijing, China, 2006.
84. Liao, M.S.; Wang, T. *Time Series InSAR Technology and Application*; Science Press: Beijing, China, 2014.
85. Ferretti, A.; Prati, C.; Rocca, F. Permanent scatterers in SAR interferometry. *IEEE Trans. Geosci. Remote Sens.* **2001**, *39*, 8–20. [CrossRef]
86. Lanari, R.; Mora, O.; Manunta, M. A small-baseline approach for investigating deformations on full-resolution differential SAR interferograms. *IEEE Trans. Geosci. Remote Sens.* **2004**, *42*, 1377–1386. [CrossRef]
87. Casu, F.; Manzo, M.; Lanari, R. A quantitative assessment of the SBAS algorithm performance for surface deformation retrieval from DInSAR data. *Remote Sens. Environ.* **2006**, *102*, 195–210. [CrossRef]
88. Li, S.; Xu, W.; Li, Z. Review of the SBAS InSAR Time-series algorithms, applications, and challenges. *Geod. Geodyn.* **2022**, *13*, 114–126. [CrossRef]
89. Farr, T.G.; Rosen, P.A.; Caro, E.; Crippen, R.; Duren, R.; Hensley, S.; Kobrick, M.; Paller, M.; Rodriguez, E.; Roth, L.; et al. The shuttle radar topography mission. *Rev. Geophys.* **2007**, *45*, G22B-0214. [CrossRef]
90. Yu, Y.H.; Balz, T.; Luo, H.; Liao, M.S.; Zhang, L. GPU accelerated interferometric SAR processing for Sentinel-1 TOPS data. *Comput. Geosci.* **2019**, *129*, 12–25. [CrossRef]
91. Duan, H.Z.; Li, Y.S.; Li, B.Q.; Li, H. Fast InSAR time-series analysis method in a full-resolution SAR coordinate system: A case study of the Yellow River Delta. *Sustainability* **2022**, *14*, 10597. [CrossRef]
92. Hanssen, R.; Bamler, R. Evaluation of interpolation kernels for sar interferometry. *IEEE Trans. Geosci. Remote Sens.* **1999**, *37*, 318–321. [CrossRef]
93. Miranda, N. Definition of the Tops SlC deramping function for products generated by the S$_{-1}$ IPF. *ESA* **2017**, 1–15.
94. Yague-Martinez, N.; Prats-Iraola, P.; Gonzalez, F.R.; Brcic, R.; Shau, R.; Geudtner, D.; Eineder, M.; Bamler, R. Interferometric Processing of Sentinel-1 TOPS Data. *IEEE Trans. Geosci. Remote Sens.* **2016**, *54*, 2220–2234. [CrossRef]
95. Li, Y.; Jiang, W.; Li, Y.; Shen, W.; He, Z.; Li, B.; Li, Q.; Jiao, Q.; Tian, Y. Coseismic Rupture Model and Tectonic Implications of the January 7 2022, Menyuan Mw 6.6 Earthquake Constraints from InSAR Observations and Field Investigation. *Remote Sens.* **2022**, *14*, 2111. [CrossRef]
96. Li, P.; Liu, L.J.; Du, J.; Xu, Y.Q.; Li, P.Y. *Monitoring and Early Warning of Typical Island Geological Hazards*; China Ocean Press: Beijing, China, 2019.
97. Li, G.; Zhao, C.; Wang, B.; Liu, X.; Chen, H. Land subsidence monitoring and dynamic prediction of reclaimed islands with multi-temporal InSAR techniques in Xiamen and Zhangzhou cities, China. *Remote Sens.* **2022**, *14*, 2930. [CrossRef]